

# Papaloizou-Pringle Instability of Magnetized Accretion Tori

Wen Fu<sup>1\*</sup> and Dong Lai<sup>1,2\*</sup>

<sup>1</sup>*Department of Astronomy, Cornell University, Ithaca, NY 14853, USA*

<sup>2</sup>*KITP, University of California, Santa Barbara, CA 93106, USA*

26 January 2014

## ABSTRACT

Hot accretion tori around a compact object are known to be susceptible to a global hydrodynamical instability, the so-called Papaloizou-Pringle (PP) instability, arising from the interaction of non-axisymmetric waves across the corotation radius, where the wave pattern speed matches the fluid rotation rate. However, accretion tori produced in various astrophysical situations (e.g., collapsars and neutron star binary mergers) are likely to be highly magnetized. We study the effect of magnetic fields on the PP instability in incompressible tori with various magnetic strengths and structures. In general, toroidal magnetic fields have significant effects on the PP instability: For thin tori (with the fractional width relative to the outer torus radius much less than unity), the instability is suppressed at large field strengths with the corresponding toroidal Alfvén speed  $v_{A\phi} \gtrsim 0.2r\Omega$  (where  $\Omega$  is the flow rotation rate). For thicker tori (with the fractional width of order 0.4 or larger), which are hydrodynamically stable, the instability sets in for sufficiently strong magnetic fields (with  $v_{A\phi} \gtrsim 0.2r\Omega$ ). Our results suggest that highly magnetized accretion tori may be subjected to global instability even when it is stable against the usual magneto-rotational instability.

**Key words:** accretion, accretion discs – hydrodynamics – instabilities – MHD

## 1 INTRODUCTION

Differentially rotating fluid flows, ubiquitous in astrophysics, can exhibit rich dynamical behaviors. Papaloizou & Pringle (1984) discovered that accretion tori can be subjected to a global non-axisymmetric instability that grows on a dynamical time-scale. Accretion tori are bagel-shaped discs with high internal temperatures and well-defined boundaries. They may be representative of certain stages or regions of the inner accretion flows around black holes, such as those found in active galactic nuclei and quasars (e.g., Begelman, Blandford & Rees 1984). They may also form in the gravitational collapse of the rotating core of massive stars (e.g., Woosley 1993) and after the merger of compact neutron star and black hole binaries (e.g., Duez et al. 2009; Etienne et al. 2009; Rezzolla et al. 2010; Montero et al. 2010), and thus are thought to be the central engine of gamma-ray bursts (e.g., Meszaros 2006). The Papaloizou-Pringle (PP) instability arises from the interaction between non-axisymmetric waves across the corotation radius ( $r_c$ ), where the wave pattern rotation frequency  $\Omega_p$  equals the background fluid rotation rate  $\Omega$  (e.g., Blaes & Glatzel 1986; Goldreich, Goodman & Narayan 1986; Glatzel 1987b). Waves outside the corotation radius ( $r > r_c$ ) have  $\Omega_p$  larger than  $\Omega(r)$  and carry positive energy, while waves at  $r < r_c$  have  $\Omega_p < \Omega(r)$  and carry negative energy. Instability occurs when the negative-energy waves inside  $r_c$  lose energy to the positive-energy waves outside  $r_c$ , leading the amplification of the wave amplitudes. To maintain the instability, the waves must be efficiently reflected at the inner and outer boundaries so that they are trapped in the torus. The growth rate of the PP instability is maximal for a constant-angular momentum torus. For a very thin torus (with the inner and outer radii close to each other), the instability disappears when  $p = d \ln \Omega / d \ln r > -\sqrt{3}$ ; for a wider torus, the instability persists (with decreasing growth rate) as the Keplerian rotation profile ( $p = -3/2$ ) is approached (e.g., Papaloizou & Pringle 1985, 1987; Goldreich et al. 1986; Zurek

\* Email: wenfu@astro.cornell.edu; dong@astro.cornell.edu

& Benz 1986; Sekiya & Miyama 1988). Other properties of the PP instability, such as its connection with the instability of vortices (e.g., Glatzel 1987a), its non-linear evolution (e.g., Goodman, Narayan & Goldreich 1987; Hawley 1991) and the effect of accretion (Blaes 1987), have been studied.

Interest in the PP instability waned in the 1990s when Balbus & Hawley (1991) pointed out that the Magneto-Rotational Instability (MRI), originally studied for magnetized Taylor-Couette flows (Velikhov 1959; Chandrasekhar 1961), can be important for astrophysical accretion discs. Since the MRI is robust and requires only a weak magnetic field, the nonlinear development of MRI may lead to efficient angular momentum transport in accretion discs. Over the last two decades, numerous studies have been devoted to the MRI and related issues such as MHD turbulence in the disc (see, e.g., Balbus & Hawley 1998 and Balbus 2003 for reviews; a sample of recent numerical studies include Hirose et al. 2009; Guan et al. 2009; Simon et al. 2009; Davis et al. 2010; Fromang 2010; Longaretti & Lesur 2010; Sorathia et al. 2010).

Nevertheless, the question remains as to what happens to the original PP instability in an accretion torus when a finite magnetic field is present. After all, the tori produced in various astrophysical situations (e.g., binary mergers; Rezzolla et al. 2010; Montero et al. 2010) are expected to be highly magnetized. One might dismiss this question as purely academic since such a magnetic torus is likely MRI unstable and therefore turbulent. We note, however, that the usual MRI operates on perturbations with vertical structure (i.e., with finite vertical wavenumber  $k_z$ ), while the PP instability operates on perturbations with  $k_z = 0$ . That is, the PP instability pertains to the height-averaged behavior of the disc. Therefore one might expect that the PP instability will continue to operate even in the presence of MRI-induced turbulence. Furthermore, in connection with Galactic black-hole X-ray binaries, it has been suggested that accretion tori can support discrete, trapped oscillation modes, which might explain high-frequency quasi-periodic oscillations (e.g., Strohmayer 2001; Remillard & McClintock 2006) observed in a number of X-ray binary systems (e.g., Rezzolla et al. 2003; Lee et al. 2004; Schnittman & Rezzolla 2006; Blaes et al. 2007; Sramkova et al. 2007; Montero et al. 2007). Although it is currently not clear that pressure-supported tori provide a realistic model for the accretion flow around a black hole in any spectral state, structures resembling pressure-supported tori do appear to be present in some non-radiative global MHD simulations of MRI-driven turbulent accretion flows (e.g., Hawley & Balbus 2002; De Villiers et al. 2003; Machida et al. 2006).

There have been a number of previous studies on global MHD instabilities in accretion flows. For example, Knobloch (1992), Kumar et al. (1994), Curry, Pudritz & Sutherland (1994) and Curry & Pudritz (1995) carried out global analysis for the axisymmetric modes with finite  $k_z$  in differentially rotating flows threaded by vertical and/or azimuthal magnetic fields, thus establishing the robustness of MRI in these flows. Ogilvie & Pringle (1996) studied the non-axisymmetric instability of a cylindrical flow containing an azimuthal field, while Curry & Pudritz (1996) studied a similar flow containing a vertical field. Both studies focused on modes with finite vertical wavenumbers, which inevitably invite MRI. Although the effect of boundaries is emphasized, a somewhat arbitrary rigid boundary condition was adopted in these studies. As far we are aware, the behavior of the PP instability for finite tori with magnetic (both vertical and azimuthal) fields has not been clarified.

In this paper, as part of our ongoing investigation of global oscillation modes and instabilities of rotating astrophysical flows (Tsang & Lai 2008, 2009a, b; Lai & Tsang 2009; Fu & Lai 2010), we carry out global stability analysis of magnetized accretion tori subjected to nonaxisymmetric perturbations. Since our main aim is to understand the effects of magnetic fields on the original PP instability, we focus on modes with no vertical structure ( $k_z = 0$ ) and we pay particular attention to the boundary conditions. As in many previous studies mentioned above, we model the torus by a cylindrical incompressible flow threaded by both vertical and toroidal magnetic fields.

Our paper is organized as follows. In section 2, we describe the equilibrium models for our rotating magnetized flows. In section 3, the basic perturbation equations are presented. We derive the boundary conditions in section 4 and present our numerical calculations of the global instability in section 5. Final summary and discussion of our results are given in section 6.

## 2 EQUILIBRIUM MODELS

As mentioned above, the PP instability operates in modes with no vertical structure ( $k_z = 0$ ). As such, the dynamics can be captured by height-averaged fluid equations. We consider a cylindrical shell (of finite width) of incompressible non-self-gravitating fluid, which is rotating differentially in the external gravitational field produced by a central compact object. We adopt the cylindrical coordinates  $(r, \phi, z)$  with the  $z$ -axis being the rotation axis. The cylindrical shell is assumed to be infinitely long in the  $z$ -direction and threaded by magnetic fields. The fluid satisfies the ideal MHD equations:

$$\frac{\partial \mathbf{u}}{\partial t} + (\mathbf{u} \cdot \nabla) \mathbf{u} = -\frac{1}{\rho} \nabla \Pi - \nabla \Phi + \frac{1}{4\pi\rho} (\mathbf{B} \cdot \nabla) \mathbf{B}, \quad (1)$$

$$\frac{\partial \mathbf{B}}{\partial t} = \nabla \times (\mathbf{u} \times \mathbf{B}), \quad (2)$$

$$\nabla \cdot \mathbf{B} = 0, \quad (3)$$

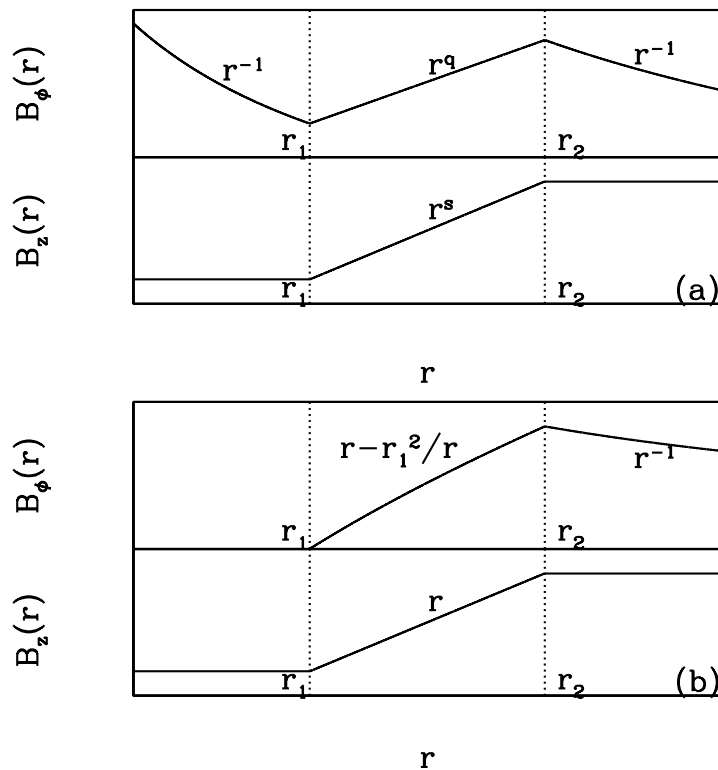


Figure 1. The two magnetic field profiles adopted in the equilibrium torus model.

$$\nabla \cdot \mathbf{u} = 0. \quad (4)$$

Here,  $\rho$  is the constant fluid density,  $\mathbf{u}$  the fluid velocity,  $\mathbf{B}$  the magnetic field, and  $\Pi = P + \mathbf{B}^2/8\pi$  the total pressure with  $P$  being the gas pressure. The gravitational potential is  $\Phi = -GM/r$ , where  $M$  is the mass of the central object. The background flow velocity  $\mathbf{u} = r\Omega(r)\hat{\phi}$  and magnetic field  $\mathbf{B} = B_\phi(r)\hat{\phi} + B_z(r)\hat{z}$  also depends only on  $r$ . For convenience, we assume the flow has a power-law rotation profile

$$\Omega(r) \propto r^p. \quad (5)$$

The flow is confined between two boundaries ( $r_1 \leq r \leq r_2$ ), where the gas pressure vanishes ( $P|_{r_1, r_2} = 0$ ). Outside the fluid zone is a vacuum devoid of matter but maybe permeated with magnetic fields. In the equilibrium state, we assume that the magnetic field is continuous across the fluid boundaries so that there is no surface electric current at  $r = r_1, r_2$  (however, we allow for surface current to develop when the fluid is perturbed). We will consider two models of magnetic field structure.

## 2.1 Model (a)

In this model, we assume that there is an external current running vertically at small radii much inside  $r_1$ , giving rise to  $B_\phi(r) \propto r^{-1}$  in the inner region ( $r < r_1$ ). There is no azimuthal current in this region, so  $B_z$  is constant. In the fluid zone, we adopt a power-law magnetic field profile

$$B_\phi(r) \propto r^q, \quad B_z(r) \propto r^s, \quad (6)$$

which means that both the azimuthal and vertical current densities are also of power-law form. Outside the fluid zone ( $r > r_2$ ), there is no current. Hence,  $B_\phi(r) \propto r^{-1}$ ,  $B_z(r) = \text{const}$ . The complete magnetic field profile is illustrated in the upper two panels of Fig. 1.

Integrating the radial equilibrium equation

$$\frac{1}{\rho} \frac{d\Pi}{dr} = -\frac{GM}{r^2} + r\Omega^2 - \frac{B_\phi^2}{4\pi\rho r}, \quad (7)$$

gives the gas pressure profile

$$\frac{P}{\rho} = \frac{GM}{r} + \frac{r^2\Omega^2}{2p+2} - \frac{1}{2}v_{Az}^2 - \frac{1}{2}\left(1 + \frac{1}{q}\right)v_{A\phi}^2 - C, \quad (8)$$

where

$$v_{Az} = B_z/\sqrt{4\pi\rho}, \quad v_{A\phi} = B_\phi/\sqrt{4\pi\rho} \quad (9)$$

are the Alfvén velocities and  $C$  is the integration constant. The location of gas pressure maximum is determined by

$$\frac{d}{dr}(P/\rho) = -\frac{GM}{r^2} - s\frac{v_{Az}^2}{r} - (1+q)\frac{v_{A\phi}^2}{r} + r\Omega^2 = 0, \quad (10)$$

which defines a reference radius  $r_0$ :

$$\frac{GM}{r_0^2} = r_0\Omega_0^2 - s\frac{v_{Az}^2(r_0)}{r_0} - (1+q)\frac{v_{A\phi}^2(r_0)}{r_0}. \quad (11)$$

Let  $C \equiv \lambda GM/r_0$  with  $\lambda$  being a constant and use Eq. (11) to substitute  $GM$  in Eq. (8), we can rewrite Eq. (8) in the dimensionless form

$$\frac{P}{\rho} = \frac{1}{r} - \lambda + \frac{r^{2p+2}}{2p+2} + sv_{Az0}^2 \left(-\frac{1}{r} + \lambda - \frac{1}{2s}r^{2s}\right) + (1+q)v_{A\phi0}^2 \left(-\frac{1}{r} + \lambda - \frac{1}{2q}r^{2q}\right), \quad (12)$$

where

$$v_{A\phi0} = v_{A\phi}(r_0)/(r_0\Omega_0), \quad v_{Az0} = v_{Az}(r_0)/(r_0\Omega_0). \quad (13)$$

Here and hereafter we will use units such that  $r_0 = \Omega_0 = 1$ . Once we specify  $p, q, s, v_{A\phi0}, v_{Az0}$  and  $\lambda$ , we can determine the locations of the torus boundary by solving  $P = 0$ . However, there are several constraints on these parameters:

(i)  $dP/dr = 0$  only guarantees the extremum of the  $P(r)$  profile. To ensure that we find a pressure maximum instead of minimum, we require  $d^2P/dr^2 < 0$  at  $r = r_0 = 1$ , which implies

$$2p + 3 - s(1 + 2s)v_{Az0}^2 - (1 + q)(1 + 2q)v_{A\phi0}^2 < 0. \quad (14)$$

This requirement reduces to  $p < -3/2$  in the  $B = 0$  limit.

(ii) Both sides of Eq. (11) need to be positive so that the gas pressure maximum exists. Thus

$$1 - sv_{Az0}^2 - (1 + q)v_{A\phi0}^2 > 0. \quad (15)$$

(iii) The maximum gas pressure  $P_{\max}$  must be positive. Thus, requiring the RHS of Eq. (12) to be positive at  $r = 1$  gives

$$\lambda < \frac{1}{1 - v_{Az0}^2 - 2v_{A\phi0}^2} \left[ \frac{2p + 3}{2p + 2} - \frac{3}{2}v_{Az0}^2 - 3v_{A\phi0}^2 \right], \quad (16)$$

provided that Eq. (15) is satisfied.

Figure 2 illustrates some examples of Model (a). We specify the values of  $p, q, s, v_{A\phi0}$  and  $v_{Az0}$ , then by varying  $\lambda$ , we obtain solutions for different torus thickness. For a given  $\Delta r/r_2$ , both  $r_1$  and  $r_2$  change when  $v_{A\phi0}$  changes as a result of magnetic support in the torus. In the hydro limit ( $v_{A\phi0} = v_{Az0} = 0$ ),  $r_1$  approaches 0.5 as  $\Delta r/r_2 \rightarrow 1$ . This feature is shown analytically in Pringle & King (2007). For a finite field strength, we see that  $r_1 \rightarrow 0$  and  $r_2 \rightarrow \infty$  as  $\Delta r/r_2 \rightarrow 1$ . Note that for a relatively thin torus ( $\Delta r/r_2 \lesssim 0.6$ ), the differences of  $r_2$  and  $r_1$  between different field strengths are quite small. Since  $B_\phi$  and  $B_z$  have similar effects on the equilibrium structure (see Eq. [12]), these features also apply to models with a finite vertical field. The special case of  $s = 0$  and  $q = -1$  is worth mentioning: In this case, the magnetic field is force-free and has no effect on the equilibrium structure<sup>1</sup>.

## 2.2 Model (b)

The magnetic field profile in this case is shown in the bottom two panels of Fig. 1. Compared with Model (a), the difference is that there is no vertical current at small radius. Therefore the azimuthal field in the inner region ( $r < r_1$ ) is zero. In the fluid zone, we assume  $B_z \propto r$  and  $B_\phi(r) \propto r - r_1^2/r$  such that both azimuthal and vertical current densities are uniform. Following the same procedure as in section 2.1, we can derive the dimensionless expression for gas pressure profile:

$$\frac{P}{\rho} = \frac{1}{r} - \lambda + \frac{r^{2p+2}}{2p+2} + v_{Az0}^2 \left( \lambda - \frac{1}{r} - \frac{1}{2}r^2 \right) + v_{A\phi0}^2 \left[ \left( \lambda - \frac{1}{r} \right) \frac{1+r_1^2}{1-r_1^2} - \frac{1}{(1-r_1^2)^2} (r^2 - r_1^2 - 2r_1^2 \ln r) \right]. \quad (17)$$

Similarly, for a viable equilibrium model to exist, the model parameters must satisfy the following requirements:

<sup>1</sup> This is why in Curry & Pudritz (1996) the one-to-one mapping between  $r_2/r_1$  and  $(r_2 - r_0)/r_2$  remains unchanged for different uniform vertical B field strengths.

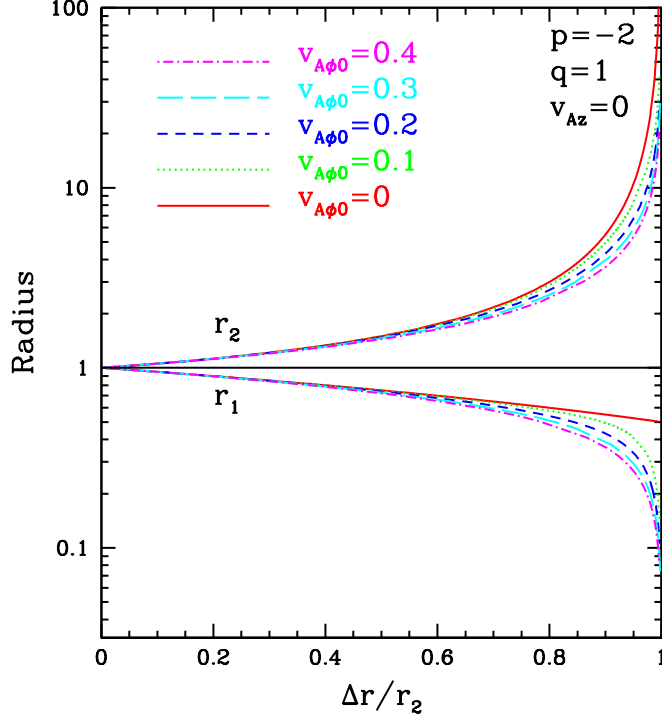


**Figure 2.** Some examples of Model (a) with a pure toroidal magnetic field ( $B_\phi \propto r$  in the fluid and  $B_z = 0$ ) and constant angular momentum distribution ( $\Omega \propto r^{-2}$ ). The x-axis is the relative thickness of the torus with  $\Delta r = r_2 - r_1$  being the absolute width, and the y-axis shows the locations of the two boundaries. The different lines represent different values of  $v_{A\phi 0} = v_{A\phi}(r_0)/(\Omega_0 r_0)$ , as indicated. The horizontal line indicates the location of gas pressure maximum ( $r_0 = 1$ ).

$$2p + 3 - 3v_{Az0}^2 - \frac{3 + r_1^4}{(1 - r_1^2)^2} v_{A\phi 0}^2 < 0, \quad (18)$$

$$1 - v_{Az0}^2 - \frac{1 + r_1^2}{1 - r_1^2} v_{A\phi 0}^2 > 0, \quad (19)$$

$$\lambda < \frac{1}{1 - v_{Az0}^2 - \frac{1 + r_1^2}{1 - r_1^2} v_{A\phi 0}^2} \left( \frac{2p + 3}{2p + 2} - \frac{3}{2} v_{Az0}^2 - \frac{2 + r_1^2}{1 - r_1^2} v_{A\phi 0}^2 \right). \quad (20)$$

### 3 MHD EQUATIONS FOR PERTURBATIONS

Assuming that the Eulerian perturbation of any physical variable  $f$  is of the form  $\delta f \propto e^{im\phi - i\omega t}$  (with no dependence on  $z$ ), the linearized perturbation equations are

$$\frac{1}{r} \frac{\partial}{\partial r} (r \delta u_r) + \frac{im}{r} \delta u_\phi = 0 \quad (21)$$

$$-i\tilde{\omega} \delta u_r - 2\Omega \delta u_\phi = -\frac{1}{\rho} \frac{\partial \delta \Pi}{\partial r} + \frac{imB_\phi}{4\pi\rho r} \delta B_r - \frac{B_\phi}{2\pi\rho r} \delta B_\phi \quad (22)$$

$$-i\tilde{\omega} \delta u_\phi + \frac{\kappa^2}{2\Omega} \delta u_r = -\frac{im}{\rho r} \delta \Pi + \frac{1}{4\pi\rho} \left( \frac{\partial}{\partial r} + \frac{1}{r} \right) B_\phi \delta B_r + \frac{imB_\phi}{4\pi\rho r} \delta B_\phi \quad (23)$$

$$-i\tilde{\omega} \delta u_z = \frac{imB_\phi}{4\pi\rho r} \delta B_z + \frac{1}{4\pi\rho} \frac{dB_z}{dr} \delta B_r \quad (24)$$

$$-i\tilde{\omega} \delta B_r = im \frac{B_\phi}{r} \delta u_r \quad (25)$$

$$-i\tilde{\omega} \delta B_\phi = \frac{imB_\phi}{r} \delta u_\phi - r \frac{d}{dr} \left( \frac{B_\phi}{r} \right) \delta u_r + r \frac{d\Omega}{dr} \delta B_r \quad (26)$$

$$-i\tilde{\omega} \delta B_z = \frac{imB_\phi}{r} \delta u_z - \frac{dB_z}{dr} \delta u_r, \quad (27)$$

where  $\tilde{\omega} = \omega - m\Omega$  is the wave frequency in the co-rotating frame and the radial epicyclic frequency  $\kappa$  is given by

$$\kappa^2 = \frac{2\Omega}{r} \frac{d}{dr}(r^2\Omega) = 2(p+2)\Omega^2. \quad (28)$$

Using  $\Delta \mathbf{u} = \delta \mathbf{u} + \boldsymbol{\xi} \cdot \nabla \mathbf{u} = d\boldsymbol{\xi}/dt = -i\omega\boldsymbol{\xi} + (\mathbf{u} \cdot \nabla)\boldsymbol{\xi}$ , we find that the Eulerian perturbation  $\delta \mathbf{u}$  is related to the Lagrangian displacement vector  $\boldsymbol{\xi}$  by  $\delta \mathbf{u} = -i\tilde{\omega}\boldsymbol{\xi} - r\Omega' \xi_r \hat{\phi}$  (prime denotes radial derivative) and we can further combine Eqs. (21)-(27) into two equations for  $\xi_r$  (radial Lagrangian displacement) and  $\delta\Pi/\rho$ :

$$\frac{d\xi_r}{dr} = A_{11}\xi_r + A_{12}\frac{\delta\Pi}{\rho}, \quad (29)$$

$$\frac{d}{dr}\left(\frac{\delta\Pi}{\rho}\right) = A_{21}\xi_r + A_{22}\frac{\delta\Pi}{\rho}, \quad (30)$$

where

$$A_{11} = -\frac{1}{r} \frac{\tilde{\omega}^2 - 2m\tilde{\omega}\Omega + m^2\omega_{A\phi}^2}{\tilde{\omega}^2 - m^2\omega_{A\phi}^2}, \quad (31)$$

$$A_{12} = \frac{m^2}{r^2}, \quad (32)$$

$$A_{21} = \tilde{\omega}^2 - m^2\omega_{A\phi}^2 - 2r\Omega \frac{d\Omega}{dr} + \left(2\frac{d\ln B_\phi}{d\ln r} - 1\right)\omega_{A\phi}^2 - 4\frac{(\tilde{\omega}\Omega + m\omega_{A\phi}^2)^2}{(\tilde{\omega}^2 - m^2\omega_{A\phi}^2)}, \quad (33)$$

$$A_{22} = \frac{2m}{r} \frac{\tilde{\omega}\Omega + m\omega_{A\phi}^2}{\tilde{\omega}^2 - m^2\omega_{A\phi}^2}, \quad (34)$$

and  $\omega_{A\phi} \equiv v_{A\phi}/r = B_\phi/(r\sqrt{4\pi\rho})$  is the toroidal Alfvén frequency. Equations (29) and (30) are the same as Eqs. (119) and (120) (derived for a pure toroidal magnetic field) in Chandrasekhar (1961).

Note that although we start with a mixed magnetic field  $\mathbf{B} = B_\phi \hat{\phi} + B_z \hat{z}$ , the final Eqs. (29) and (30) do not contain  $B_z$ . The reason is that the  $z$ -component only appears in Eqs. (24) and (27), which in fact can be decoupled from the other five perturbation equations. Indeed, using Eq. (25) to replace  $\delta B_r$  in Eq. (24), and combining with Eq. (27), we find

$$(\tilde{\omega}^2 - m^2\omega_{A\phi}^2) \left( \delta B_z + \frac{i}{\tilde{\omega}} \frac{dB_z}{dr} \delta u_r \right) = 0. \quad (35)$$

In general,  $\tilde{\omega}^2 - m^2\omega_{A\phi}^2 \neq 0$ . Comparing the above equation with Eq. (27) we have  $\delta u_z = 0$ . This is to be expected since the perturbed quantities are assumed to be independent of  $z$ . Also note that when the wave frequency  $\omega$  is real, the coefficients  $A_{11}$ ,  $A_{21}$  and  $A_{22}$  are singular at

$$\tilde{\omega}^2 = m^2\omega_{A\phi}^2. \quad (36)$$

We shall call them the Magnetic Resonances (MRs). Obviously, they reduce to the corotation resonance when  $B_\phi = 0$ .

#### 4 BOUNDARY CONDITIONS

In general, the boundary of any magnetized flow should satisfy the following conditions:

$$[\rho u_n] = 0, \quad (37)$$

$$[\mathbf{n} \cdot \mathbf{B}] = 0, \quad (38)$$

$$\left[ P + \rho u_n^2 + \frac{B_t^2}{8\pi} \right] = 0, \quad (39)$$

$$\left[ \rho u_n \mathbf{u}_t - \frac{B_n \mathbf{B}_t}{4\pi} \right] = 0, \quad (40)$$

where  $\mathbf{n}$  is a unit vector normal to the boundary surface, the subscript  $n$  and  $t$  denote the normal and tangential components, and the square bracket represents the difference in a quantity across the boundary (e.g., Schmidt 1979; Shu 1992). For the system we study in this paper, there is no radial background flow, we only need to consider Eqs. (38)-(40) with  $u_n = 0$ . Obviously, with the magnetic field continuous across the boundaries and with no radial field component, our equilibrium models constructed in Sec. 2 already satisfy the boundary conditions. In the perturbed state, the boundary conditions read

$$\Delta[\mathbf{n} \cdot \mathbf{B}] = 0, \quad (41)$$

$$\Delta \left[ P + \frac{B_t^2}{8\pi} \right] = 0, \quad (42)$$

$$\Delta \left[ \frac{B_n \mathbf{B}_t}{4\pi} \right] = 0. \quad (43)$$

Note that  $\Delta[\mathbf{n} \cdot \mathbf{B}] = [(\Delta \mathbf{n}) \cdot \mathbf{B}] + [\mathbf{n} \cdot \Delta \mathbf{B}]$ , and since both  $\mathbf{n}$  and  $\Delta \mathbf{n}$  are the same across the boundary<sup>2</sup>, Eq. (41) simply becomes  $\mathbf{n} \cdot [\Delta \mathbf{B}] = 0$ , where we have used  $[\mathbf{B}] = 0$  (as assumed in our model setup). Since  $(\Delta \mathbf{B})_r = (\delta \mathbf{B} + \boldsymbol{\xi} \cdot \nabla \mathbf{B})_r = \delta B_r - \xi_\phi B_\phi / r$ , and both  $\xi_\phi$  and  $B_\phi$  are continuous across the boundaries, we find

$$[\delta B_r] = 0. \quad (44)$$

On the other hand, Eqs. (41) and (42) combine to give

$$[\Delta \Pi] = 0. \quad (45)$$

The condition (43) is already satisfied because  $\Delta [B_n \mathbf{B}_t] = [(\Delta B_n) \mathbf{B}_t] + [B_n \Delta \mathbf{B}_t] = 0$  when the background field is continuous. We note that the perturbed magnetic field does not need to be continuous across the boundary. This means that there could be surface current induced by the perturbation.

To implement the two boundary conditions (44)-(45), we need to calculate the perturbed magnetic field in the vacuum region ( $r < r_1$  and  $r > r_2$ ). This can be done by solving

$$\nabla \times \delta \mathbf{B} = 0, \quad \nabla \cdot \delta \mathbf{B} = 0. \quad (46)$$

Clearly,  $\delta \mathbf{B}$  is a potential field  $\delta \mathbf{B} = \nabla \Psi$  with  $\Psi$  (also  $\propto e^{im\phi - i\omega t}$ ) satisfying

$$\nabla^2 \Psi = 0. \quad (47)$$

The solution of Eq. (47) is

$$\Psi = C_1 r^m + C_2 r^{-m}, \quad (48)$$

where  $C_1$  and  $C_2$  are integration constants. Requiring  $\delta \mathbf{B}$  to be regular at  $r \rightarrow 0$  and  $r \rightarrow \infty$ , we find

$$\delta B_r = C_1 m r^{m-1}, \quad \delta B_\phi = C_1 \frac{im}{r} r^m, \quad \text{for } r < r_1, \quad (49)$$

and

$$\delta B_r = -C_2 m r^{-m-1}, \quad \delta B_\phi = C_2 \frac{im}{r} r^{-m}, \quad \text{for } r > r_2. \quad (50)$$

The two constants  $C_1$  and  $C_2$  can be determined by using  $[\delta B_r] = 0$ . At  $r = r_1$ , this implies  $C_1 m r^{m-1} = im B_\phi \xi_r / r$  (see Eq. [25] for  $\delta B_r$  inside the fluid zone). Thus,

$$C_1 = i B_\phi \xi_r r^{-m} |_{r_1}. \quad (51)$$

Similarly,

$$C_2 = -i B_\phi \xi_r r^m |_{r_2}. \quad (52)$$

Since the detailed realization of the boundary condition  $[\Delta \Pi] = 0$  depends on the specific equilibrium model, we address the two models separately.

#### 4.1 Model (a)

At the inner boundary  $r = r_1$ , by using Eq. (51), we find that the Lagrangian perturbation of the total pressure in the vacuum just inside  $r_1$  (i.e.,  $r = r_{1-}$ ) is given by

$$\Delta \Pi |_{r_{1-}} = \frac{B_\phi \delta B_\phi}{4\pi} - \xi_r \frac{B_\phi^2}{4\pi r} = -(m+1) \xi_r \frac{B_\phi^2}{4\pi r}. \quad (53)$$

In the fluid just outside  $r_1$  (i.e.,  $r = r_{1+}$ ), we have

$$\Delta \Pi |_{r_{1+}} = \delta \Pi + \xi_r \left[ r^{2p+1} - \frac{v_{A\phi}^2}{r} - \frac{1}{r^2} (1 - s v_{Az0}^2 - (1+q) v_{A\phi 0}^2) \right] \rho. \quad (54)$$

Thus the condition  $[\Delta \Pi] = 0$  at  $r = r_1$  can be written as

$$\frac{\delta \Pi}{\rho} + \xi_r \left[ r^{2p+1} + \frac{m v_{A\phi}^2}{r} - \frac{1}{r^2} (1 - s v_{Az0}^2 - (1+q) v_{A\phi 0}^2) \right] = 0, \quad \text{at } r = r_{1+}. \quad (55)$$

Note that in deriving the above equation, we have implicitly used  $[B_\phi] = 0$  and  $[\xi_r] = 0$ . The same procedure yields the boundary condition at  $r = r_2$

<sup>2</sup> Note that in the non-axisymmetric case, the perturbed surface normal vector  $\Delta \mathbf{n}$  is not the same as  $\hat{\mathbf{r}}$ ; see Schmidt (1979) for a derivation of  $\Delta \mathbf{n}$ .

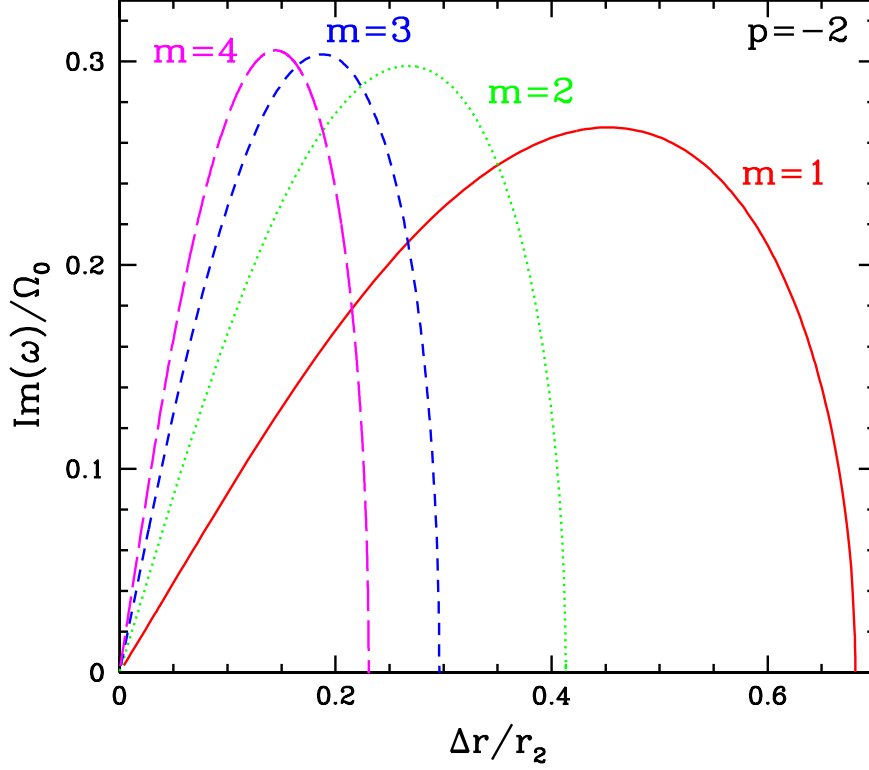


**Figure 3.** The growth rate of Papaloizou-Pringle instability (in units of  $\Omega_0$ , the fluid rotation rate at the pressure maximum of the torus) as a function of the relative thickness of the torus for different values of  $m$ . The rotation profile is  $\Omega \propto r^{-2}$ . This figure is similar to Fig. 1 in Blaes & Glatzel (1986) and to Fig. 1 in Abramowicz et al. (1987).

$$\frac{\delta\Pi}{\rho} + \xi_r \left[ r^{2p+1} - \frac{mv_{A\phi}^2}{r} - \frac{1}{r^2} (1 - sv_{Az0}^2 - (1+q)v_{A\phi 0}^2) \right] = 0, \quad \text{at } r = r_{2-}. \quad (56)$$

#### 4.2 Model (b)

The derivation is similar to Model (a). In this case, the boundary conditions are

$$\frac{\delta\Pi}{\rho} + \xi_r \left[ r^{2p+1} - \frac{1}{r^2} \left( 1 - v_{Az0}^2 - \frac{1+r_1^2}{1-r_1^2} v_{A\phi 0}^2 \right) \right] = 0, \quad \text{at } r = r_{1+}, \quad (57)$$

$$\frac{\delta\Pi}{\rho} + \xi_r \left[ r^{2p+1} - \frac{mv_{A\phi 0}^2}{(1-r_1^2)^2} \left( 1 - \frac{r_1^2}{r^2} \right) - \frac{1}{r^2} \left( 1 - v_{Az0}^2 - \frac{1+r_1^2}{1-r_1^2} v_{A\phi 0}^2 \right) \right] = 0, \quad \text{at } r = r_{2-}. \quad (58)$$

## 5 NUMERICAL RESULTS

We employ the standard shooting method (Press et al. 1992) to solve Eqs. (29) and (30) subjected to the boundary conditions (55)-(56) [Model (a)] or (57)-(58) [Model (b)] to obtain the eigenvalue  $\omega = \omega_r + i\omega_i$ . For most of our analysis, we set the rotation index  $p = -2$  (i.e.,  $\Omega \propto r^{-2}$ ) such that our results can be directly compared with the original Papaloizou-Pringle instability.

Before discussing our results for finite magnetic fields, we briefly review the main features of the classical (hydrodynamical) PP instability. As seen in Fig. 3, the instability growth rate increases with increasing torus thickness for small  $\Delta r/r_2$  but terminates at some finite thickness. As  $m$  increases, the termination point shifts to smaller  $\Delta r/r_2$ , although the peak growth rate remains approximately the same. This means that the PP instability only exists for relatively thin tori, as shown by Blaes



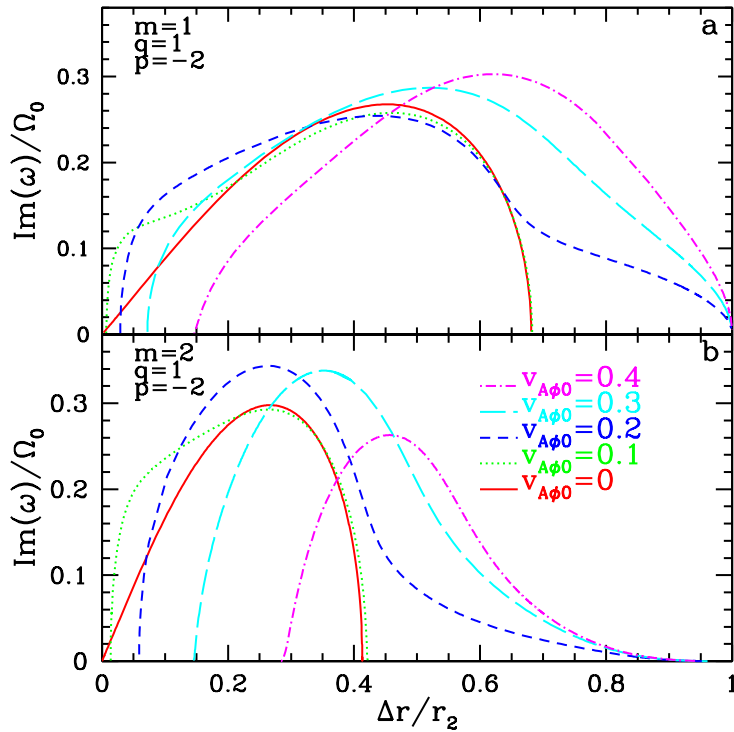


**Figure 4.** The instability growth rate as a function of the relative thickness of the torus for a range of toroidal magnetic field strengths. Different lines represent different  $v_{A\phi 0}$  with the solid line denoting the hydrodynamic case. The upper and bottom panels are for the  $m = 1$  and  $m = 2$  modes, respectively.

& Glatzel (1986) and by Abramowicz et al. (1987). The former also provides an approximate analytical expression for the limiting maximum growth rate as  $m \rightarrow \infty$ . These features can be understood from the fact that the PP instability arises from the interaction of the surface gravity waves at the torus boundary. For a thin torus, the velocity shear across the corotation point is small, and there would not be enough shear rotational energy available to drive the growth. When the torus thickness is too large, the wave amplitudes at the corotation radius (where the waves exchange angular momentum) is too small to allow for adequate interactions. Thus, only for the “intermediate” torus thickness, with  $m\Delta r/r \lesssim 1$ , will the instability operate. This explains why for a larger  $m$ , the PP instability terminates at a smaller torus thickness.

### 5.1 Model (a): Pure Toroidal Field Configuration

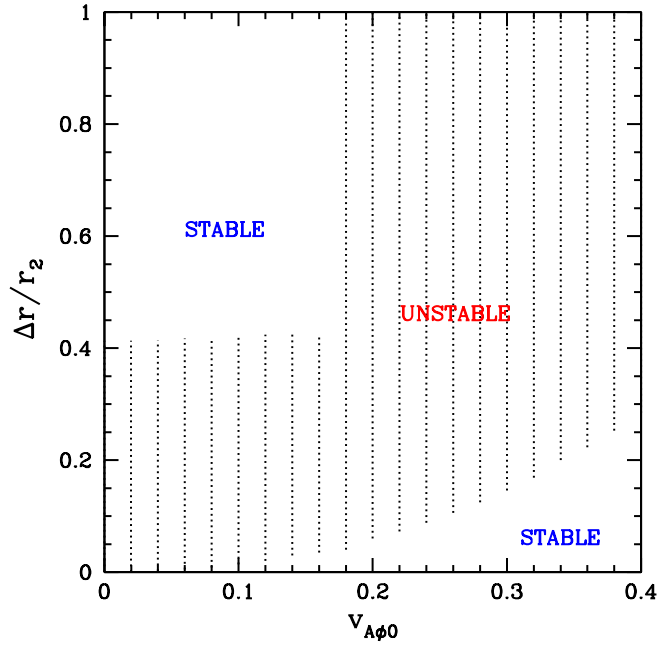
In this section, we present the numerical results for an accretion torus with a pure power-law profile toroidal magnetic field. We choose the power-law index  $q = 1$  so that the vertical current density is uniform as in Model (b).

Figure 4 shows the growth rate  $\omega_i$  as a function of thickness  $\Delta r/r_2$  for different  $v_{A\phi 0}$ . The two panels share similar characteristics: (i) For relatively weak B field ( $v_{A\phi 0} \lesssim 0.1$ ), the instability resembles the  $B = 0$  limit in that it always starts from infinitely small thickness and terminates beyond a certain  $\Delta r/r_2$ ; (ii) For stronger B fields, the instability starts beyond certain finite  $\Delta r/r_2$  and then extends all the way to very large thickness (although as  $\Delta r/r_2$  approaches unity, the growth rate becomes increasingly small). As  $v_{A\phi 0}$  increases, the critical thickness for the onset of instability also increases.

Figure 5 maps out the unstable zone in the thickness – magnetic field strength parameter space. It shows the similar feature as as Fig. 4. We can see that the unstable region is mainly located at the lower-left (thin torus with weak B field) and the upper-right (thicker torus with strong B field) corners of the parameter space.

In Fig. 6, we present our numerical results in a different way. We fix the dimensionless thickness  $\Delta r/r_2$  and plot the growth rate as a function of magnetic field strength. For a thin torus, we find that as  $v_{A\phi 0}$  increases, the growth rate first goes up slightly compared to the  $B = 0$  case, then decreases and becomes completely suppressed when the magnetic field is sufficiently strong ( $v_{A\phi}$  comparable to rotation velocity). For a thick torus, the instability can survive for a relatively stronger B field and then vanishes beyond a certain  $v_{A\phi 0}$ .

To probe the underlying physics of how magnetic fields affect the PP instability, we show in Fig. 7 the locations of several special points in the fluid: The corotation radius  $r_c$  is where the wave pattern corotates with the background flow, i.e.,  $\tilde{\omega}_r = \omega_r - m\Omega = 0$ . The inner/outer magnetic resonances (IMR/OMR) are defined by [see Eq. (36)]



**Figure 5.** The instability region in the parameter space defined by the dimensionless torus thickness  $\Delta r/r_2$  and the toroidal magnetic field strength. The other parameters are fixed to  $m = 2$ ,  $\Omega \propto r^{-2}$  and  $B_\phi \propto r$ . The dotted area denotes the region where a growing mode can be found.

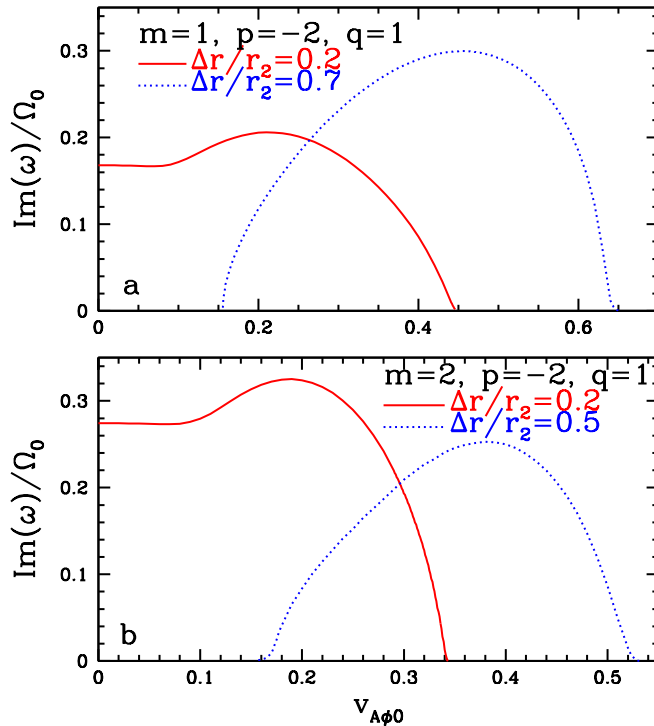


**Figure 6.** The instability growth rate as a function of  $v_{A\phi 0} = v_{A\phi}(r_0)/(r_0\Omega_0)$  for tori with different thickness  $\Delta r/r_2$ . The upper and bottom panels depict the cases with  $m = 1$  and  $m = 2$ , respectively.

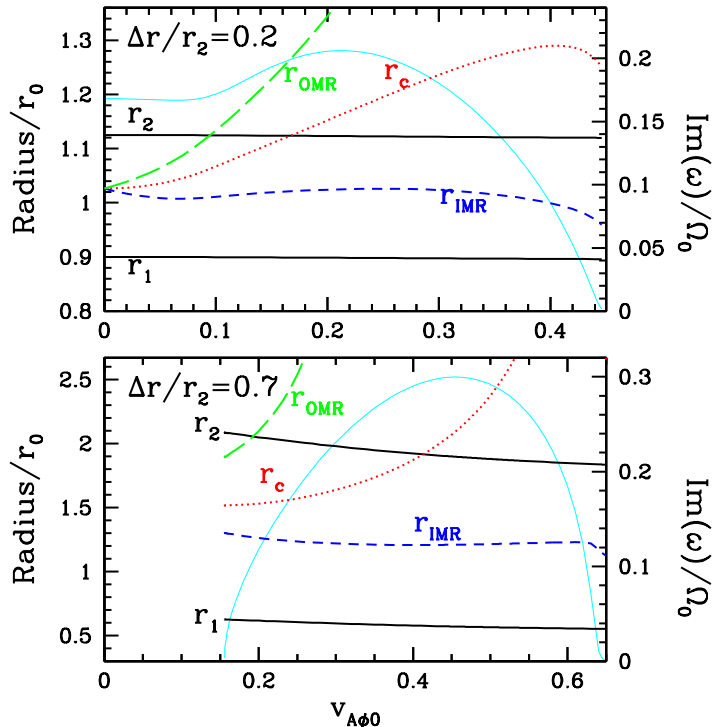


**Figure 7.** Some special radii for the  $m = 1$  overstable mode in a torus as a function of the dimensionless magnetic field strength  $v_{A\phi 0}$ . The upper and bottom panels correspond to a thin ( $\Delta r/r_2 = 0.2$ ) and thick ( $\Delta r/r_2 = 0.7$ ) torus, respectively. The two solid lines show the inner and outer torus boundaries ( $r_1$  and  $r_2$ ). The dotted line represents the corotation radius, while the shot-dashed and long-dashed lines show the inner and outer magnetic resonances (IMR and OMR), respectively [see Eq. (59)]. The thin solid line is the mode growth rate with the scale shown on the right. The torus rotation and magnetic field profiles are  $\Omega \propto r^{-2}$  and  $B_\phi \propto r$ .

$$\tilde{\omega}_r = \omega_r - m\Omega = \pm m\omega_{A\phi}. \quad (59)$$

At the IMR, the wave is trailing the background flow but corotates with the azimuthal Alfvén wave traveling in the counter-rotational direction (viewed in the corotating frame), while at the OMR, the wave is leading the background flow and corotates with the Alfvén wave in the rotational direction. Recall that for PP instability to operate in the  $B = 0$  limit, it is essential that the corotation radius lies in between torus boundaries (i.e.,  $r_1 < r_c < r_2$ ). Now, with the inclusion of the magnetic field, we see from Fig. 7 that as  $v_{A\phi 0}$  increases, both  $r_c$  and  $r_{\text{OMR}}$  shift beyond the outer boundary of the torus. The IMR radius,  $r_{\text{IMR}}$ , however, always stays inside the fluid. This suggests that in a magnetic torus, the IMR plays a similar role as the corotation resonance does in a non-magnetic torus.

## 5.2 Other Magnetic Field Configurations

### 5.2.1 Model (a): Mixed magnetic field

Although the vertical magnetic field  $B_z$  does not enter into the perturbation equations, the presence of a finite  $B_z$  can affect the mode growth rate through the boundary conditions. Figure 8 shows some results for the accretion tori with a mixture of vertical and toroidal magnetic fields. We take the power-law index of  $B_z$  to be  $s = 1$  so that the azimuthal electric current density is constant. In Fig. 8, we fix the toroidal field and plot the mode growth rate as a function of the vertical field strength. We find that the effect of finite  $v_{Az 0}$  is small (note the scale of the y-axis). For  $v_{Az} = 0$ , the results agree with what is shown in Fig. 6b.

### 5.2.2 Model (b): Pure toroidal field

In this case, since the background toroidal magnetic field has a profile that depends on the inner boundary radius  $r_1$ , to solve for the equilibrium structure and the global mode, we must first specify  $r_1$ . Once we fix  $r_1$ , we can easily solve for the other boundary radius  $r_2$ . In Fig. 9, we show in the upper panel the mode growth rate as a function of  $v_{A\phi 0}$ . The result is qualitatively similar to Fig. 6b. The bottom panel shows that for a fixed inner boundary radius  $r_1$ , the thickness does not

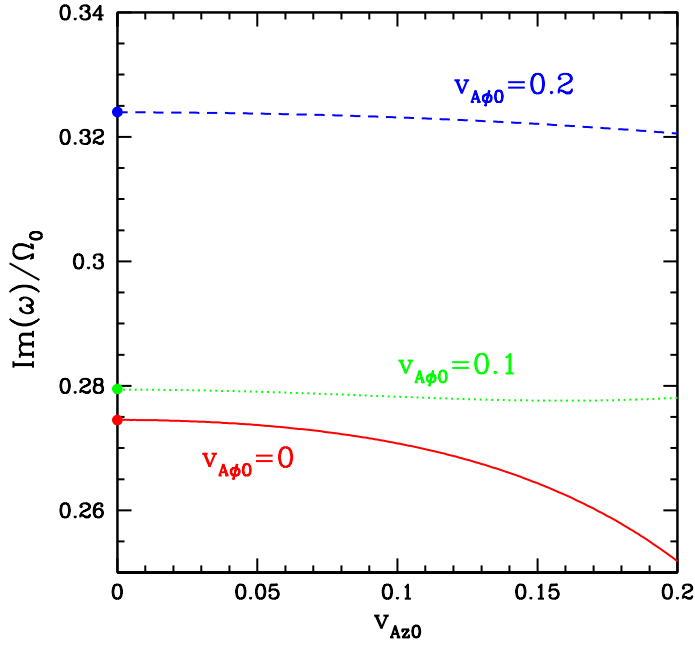


**Figure 8.** The instability growth rate as a function of  $v_{Az0}$  for a torus with relative thickness  $\Delta r/r_2 = 0.2$ . Different lines represent different values of  $v_{A\phi 0}$ . The other parameters are fixed to  $m = 2$ ,  $\Omega \propto r^{-2}$ ,  $B_\phi \propto r$  and  $B_z \propto r$  in the fluid.

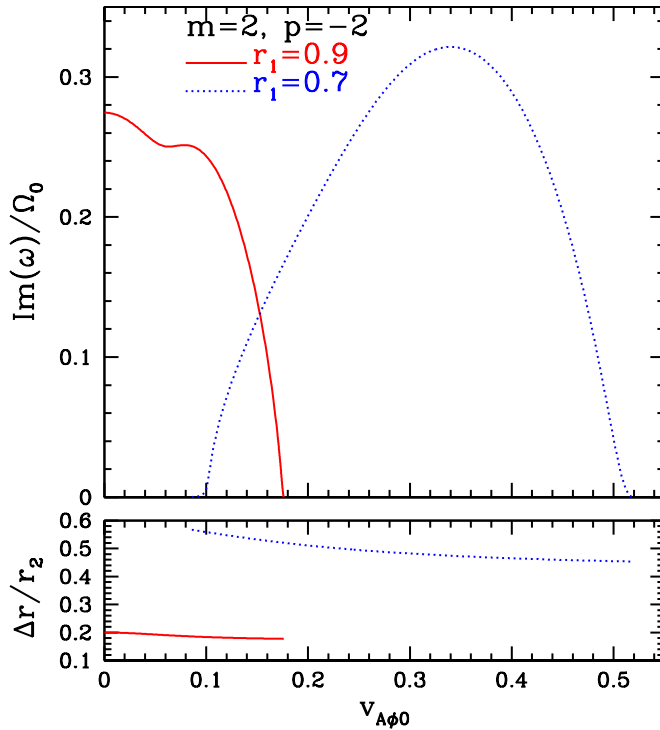


**Figure 9.** The instability growth rate as a function of  $v_{A\phi 0}$  for accretion tori described by Model (b) with a pure toroidal magnetic field. The solid and dotted lines correspond to two different inner disc boundary radii. The bottom pane shows the corresponding torus relative thickness.

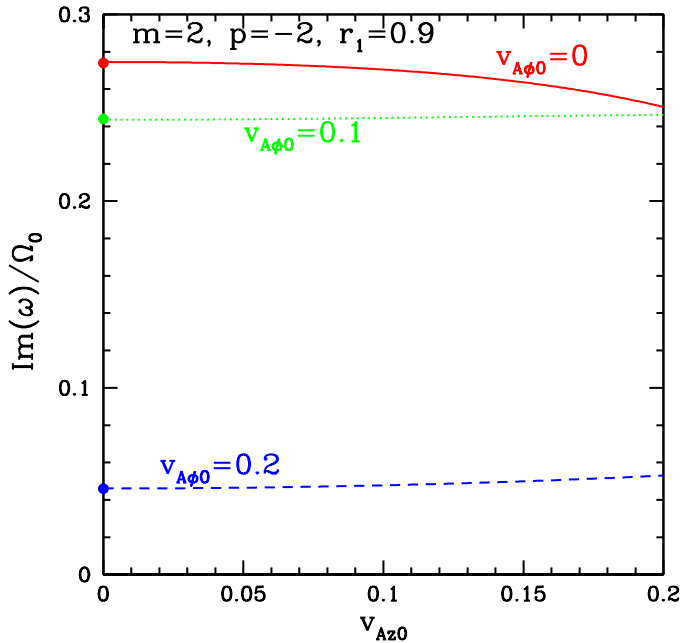


**Figure 10.** The instability growth rate as a function of  $v_{Az0}$  for a thin torus (with  $r_1 = 0.9$  and  $\Delta r/r_2 \simeq 0.2$ ). The different lines represent different values of  $v_{A\phi 0}$ . Unlike Fig. 8, here the magnetic field profile is described by Model (b).

change appreciably as  $v_{A\phi 0}$  varies. So the two values of  $r_1$  we choose adequately depict the thin and thick tori, respectively. Again, we see that for a thin torus, the original Papaloizou-Pringle instability is suppressed by the toroidal field, while for a thick torus, the instability can survive for larger field strengths.

### 5.2.3 Model (b): Mixed magnetic field

In Fig. 10, we show the mode growth rate as a function of  $v_{Az0}$  for different fixed values of  $v_{A\phi 0}$ . Similar to the case shown in Fig. 8, we see that the vertical magnetic field has a small effect on the stability property of a magnetized accretion torus. Again, this is understandable given that  $B_z$  does not enter into the differential equations for the perturbations, but only affects the modes through boundary conditions.

## 6 DISCUSSION

In this paper, we have studied the effect of magnetic fields on the global non-axisymmetric instability (the PP instability) in accretion tori. For simplicity, we assume that both the perturbation and the background flow variables have no  $z$ -dependence (thus our tori are essentially 2D cylinders). We have explored various possible magnetic configurations in the torus. Although the detailed property of the instability is model-dependent, Figs. 4-6 illustrate our general findings: (i) For thin tori (with the dimensionless thickness  $\Delta r/r_2 \lesssim 0.2$ , where  $r_2$  is the outer torus radius), the instability exists for zero and weak magnetic fields, but is suppressed when the toroidal field becomes sufficiently strong (with the corresponding Alfvén speed  $v_{A\phi} \gtrsim 0.2r\Omega$  measured at gas pressure maximum); (ii) For thicker tori ( $\Delta r/r_2 \gtrsim 0.4$ ), the PP instability does not operate for zero and weak magnetic fields, but becomes active when the field is sufficiently strong ( $v_{A\phi} \gtrsim 0.2r\Omega$  measured at gas pressure maximum). A vertical magnetic field also influences the PP instability, but its effect is generally smaller than that of the toroidal field.

It is difficult to precisely pin down the physical origin of the magnetic field effect on the PP instability. For example, with a finite toroidal magnetic field, we find that the corotation resonance radius may lie outside the torus body, and yet the torus is still unstable. On the other hand, the inner magnetic resonance radius, where  $\omega_r - m\Omega = -m\omega_{A\phi}$  [see Eq. (59)], always lie inside the fluid body. Thus we suspect that in a magnetic torus, the inner magnetic resonance plays a similar role as the corotation resonance does in a non-magnetic torus.

We note that the PP instability (or its magnetic generalization) involves wave modes that do not have vertical structure

(i.e.  $k_z = 0$ ). Thus it is distinctly different from the usual MRI (Balbus & Hawley 1998). Our finding about the instability of think tori with strong magnetic fields is particularly interesting: Since the MRI can be suppressed when the magnetic field is too strong, our results suggest that magnetized tori may be subject to the instability even when it is stable against the usual MRI.

## ACKNOWLEDGMENTS

We thank Thierry Foglizzo, Omer Blaes and David Tsang for useful discussion during the course of this study. This work has been supported in part by NASA Grant NNX07AG81G and NSF grants AST 0707628. DL also acknowledges the hospitality (January - June, 2010) of the Kavli Institute for Theoretical Physics at UCSB, funded by the NSF through grant PHY05-51164.

## REFERENCES

- Abramowicz, M. A., Blaes, O. M. & Ghosh, P., 1987, *ApJ*, 323, 629  
 Balbus, S. A., 2003, *ARAA*, 41, 555  
 Balbus, S. A. & Hawley, J. F., 1991, *ApJ*, 376, 214  
 Balbus, S. A. & Hawley, J. F., 1998, *Rev. Mod. Phys.*, 70, 1  
 Begelman, M. C., Blandford, R. D. & Rees, M. J., 1984, *Rev. Mod. Phys.*, 56, 255  
 Blaes, O. M., 1987, *MNRAS*, 227, 975  
 Blaes, O. M. & Glatzel, W., 1986, *MNRAS*, 220, 253  
 Blaes, O. M., Sramkova, E., Abramowicz, M. A., Kluzniak, W. & Torkelsson, U., 2007, *ApJ*, 665, 642  
 Chandrasekhar S., 1961, *Hydrodynamic and Hydromagnetic Stability*, Oxford University Press  
 Curry, C., Pudritz, R. E. & Sutherland, P. G., 1994, *ApJ*, 434, 206  
 Curry, C. & Pudritz, R. E., 1995, *ApJ*, 453, 697  
 Curry, C. & Pudritz, R. E., 1996, *MNRAS*, 281, 119  
 Davis, S. W., Stone, J. M. & Pessah, M. E., 2010, *ApJ*, 713, 52  
 De Villiers, J. P., Hawley, J. F., & Krolik, J. H., 2003, *ApJ*, 599, 1238  
 Duez, M., Foucart, F., Kidder, L. E., Ott, C. D. & Teukolsky, S. A., 2010, *Class. Quantum Grav.*, 27, 114106  
 Etienne, Z. B., Liu, Y. T., Shapiro, S. L. & Baumgarte, T. W., 2009, *Phys. Rev. D*, 79, 044024  
 Fromang, S., 2010, *A&A*, 514, L5  
 Fu, W. & Lai, D., 2010, *MNRAS*, submitted  
 Glatzel, W., 1987a, *MNRAS*, 225, 227  
 Glatzel, W., 1987b, *MNRAS*, 228, 77  
 Goldreich, P., Goodman, J. & Narayan, R., 1986, *MNRAS*, 221, 339  
 Goodman, J., Narayan, R. & Goldreich, P., 1987, *MNRAS*, 225, 695  
 Guan, X., Gammie, C. F., Simon, J. B. & Johnson, B. M., 2009, *ApJ*, 694, 1010  
 Hawley, J. F., 1991, *ApJ*, 381, 496  
 Hawley, J. F., & Balbus, S. A. 2002, *ApJ*, 573, 738  
 Hirose, S., Blaes, O. & Krolik, J. H., 2009, *ApJ*, 704, 781  
 Knobloch, E., 1992, *MNRAS*, 255, 25p  
 Kumar, S., Coleman, C. S. & Kley, W., 1994, *MNRAS*, 266, 379  
 Lai, D. & Tsang, D., 2009, *MNRAS*, 393, 979  
 Lee, W. H., Abramowicz, M. A. & Kluziniak, W., 2004, *ApJ*, 603, L93  
 Longaretti, P. -Y. & Lesur, G., 2010, arXiv:1004.1384  
 Meszaros, P., 2006, *Rep. Prog. Phys.*, 69, 2259  
 Montero, P. J., Zanotti, O., Font, J. A. & Rezzolla, L., 2007, *MNRAS*, 378, 1101  
 Montero, P. J., Font, J. A. & Shibata, M., 2010, *Phys. Rev. Lett.*, 104, 191101  
 Machida, M., Nakamura, K. E., & Matsumoto, R., 2006, *PASJ*, 58, 193  
 Ogilvie, G. I. & Pringle, J. E., 1996, *MNRAS*, 279, 152  
 Papaloizou, J. C. B. & Pringle, J. E., 1984, *MNRAS*, 208, 721  
 Papaloizou, J. C. B. & Pringle, J. E., 1985, *MNRAS*, 213, 799  
 Papaloizou, J. C. B. & Pringle, J. E., 1987, *MNRAS*, 225, 267  
 Press, W. H., Teukolsky, S. A., Vetterling, W. T. & Flannery, B. P., 1992, *Numerical Recipes*, Cambridge University Press  
 Pringle, J. & King, A., 2007, *Astrophysical Flows*, Cambridge University Press  
 Remillard, R. A. & McClintock, J. E., 2006, *ARAA*, 44, 49  
 Rezzolla, L., Yoshida, S., Maccarone, T. J. & Zanotti, O., 2003, *MNRAS*, 344, L37

- Rezzolla, L., Baiotti, L., Giacomazzo, B., Link, D. & Font, J. A., 2010, *Class. Quantum Grav.*, 27, 114105
- Schmidt, G., 1979, *Physics of High Temperature Plasmas*, Academic Press
- Schnittman, J. D. & Rezzolla, L., 2006, *ApJ*, 637, L113
- Sekiya, M. & Miyama, S. M., 1988, *MNRAS*, 234, 107
- Shu, F. H., 1992, *Gas Dynamics*, University Science Books
- Simon, J. B., Hawley, J. F. & Beckwith, K., 2009, *ApJ*, 690, 974
- Sorathia, K. A., Reynolds, C. S. & Armitage, P. J., 2010, *ApJ*, 712, 1241
- Strohmer, T. E., 2001, *ApJ*, 552, L49
- Sramkova, E., Torkelsson, U. & Abramowicz, M. A., 2007, *A&A*, 467, 641
- Tsang, D. & Lai, D., 2008, *MNRAS*, 387, 446
- Tsang, D. & Lai, D., 2009a, *MNRAS*, 393, 992
- Tsang, D. & Lai, D., 2009b, *MNRAS*, 400, 470
- Velikhov, E. P., 1959, *Sov. Phys. JETP* 36, 995
- Woosley, S. E., 1993, *ApJ*, 405, 273
- Zurek, W. H. & Benz, W., 1986, *ApJ*, 308, 132